POAC'25
St. John's,
Newfoundland and
Labrador, Canada

Proceedings of the 28th International Conference on
Port and Ocean Engineering under Arctic Conditions
Jul 13-17, 2025
St. John's, Newfoundland and Labrador
Canada

Dynamic analysis of six-degrees-of-freedom motion in wave energy converters

Saroj Gautam[1], Kevin Pope[1], Baafour Nyantekyi-Kwakye[2]
[1] Memorial University of Newfoundland, Canada
[2] Dalhousie University, Halifax, Nova Scotia, Canada

ABSTRACT

This study investigated the six-degrees-of-freedom dynamic motion of oscillating point absorber-type wave energy converter (WEC) subjected to wave-induced forces. In this study, the Reynolds-averaged Navier-Stokes-based numerical technique with the volume of fluid method was employed to capture the air-water interface interactions. The investigation of WEC motion showed the predominant vertical motion along with motions in spanwise and streamwise directions but with lower amplitude. The results also highlight the contribution of viscous forces that can influence energy dissipation and structural stresses. Wake and vortex formations were identified near the air-water interface, which enhances viscous dissipation and affects hydrodynamic forces and energy efficiency. Despite the smaller magnitude, these viscous forces can be incorporated to optimize the power take-off system for improved energy capture.

KEY WORDS: Degree-of-freedom; RANS; viscous force; VoF; wave energy converter

INTRODUCTION

Due to the increasing demand for sustainable energy and the limitations of fossil fuel-based power generation, global efforts have turned towards harnessing ocean energy through wave energy converters (WECs). WECs are devices designed to harness the energy of ocean waves and convert it into usable electricity. Among the various types of WECs, point absorbers are characterized by their compact geometry and their ability to operate efficiently across a range of sea states(Li and Yu, 2012; Shadman et al., 2018). As waves pass, the device oscillates most commonly in the vertical direction, which is used to drive a power take-off system. Wave energy presents a vast and largely untapped resource, offering a continuous and predictable power supply compared to other renewable sources (Gallutia et al., 2022; Lehmann et al., 2017). Energy capture in varying sea states requires a detailed understanding of the hydrodynamic interactions of WECs. By refining design parameters and improving control strategies, oscillating water body WECs can enhance energy extraction and contribute to the broader adoption of wave energy as a reliable renewable source. A six-degree-of-freedom (6-DoF) oscillating point absorber-type WEC offers improvements in energy-capturing efficiency (Galván-Pozos and Ocampo-Torres, 2020; Vervaet et al., 2022). The ability to move in all six degrees of freedom allows the WEC to respond more effectively to wave forces from multiple directions, maximizing energy absorption across different sea conditions.

Numerical models based on computational fluid dynamics (CFD) are required to achieve high-fidelity predictions, as boundary element method (BEM) solvers cannot fully capture nonlinear and viscous flow effects (Penalba et al., 2018). Studies have shown that extending WEC motion to 6-DoF can improve the accuracy of wave-body interaction predictions, including in the event of extreme wave conditions (Ransley et al., 2017a). (Ransley et al., 2017b) developed a numerical model using an incompressible volume of fluid (VoF) method combined with a second-order wave model and a 6-DoF solver to simulate the WEC motions. Their study was able to capture the dynamic interactions, including the free surface effect, wave scattering, and device motion under different wave conditions. (Yang et al., 2023) utilized a dynamic fluid-body interaction scheme with a k-ε turbulence model for WEC simulations. Although such a study is effective for uniform wave conditions, the simpler turbulence models limited the ability to capture the flow field on a large scale.

Results from previous studies have emphasized the need for high-resolution modeling techniques with better turbulence models for more accurate simulations of WEC behavior. By leveraging improved numerical modeling and optimizing WIEC design, energy extraction can be enhanced, making wave energy a more viable and efficient renewable energy source. This study investigates the 6-DoF motion of a hemispherical-cylinder point absorber to examine the non-linear responses. The study examines the primary energy-producing motions (surge, heave, and pitch) and their associated wave excitation forces, coupled with secondary motions (sway, roll, and yaw) induced by wave-structure interactions. The numerical technique has been used with Stokes 2$^{\text{nd}}$-order waves condition to capture nonlinear phenomena, including wave overwash and vortex shedding.

FORMULATION OF NUMERICAL PREDICTION

Governing Equations and Boundary Conditions

For the numerical modeling of incompressible fluid flow, the conservation of mass and momentum is formulated through the Reynolds-Averaged Navier–Stokes (RANS) equations Eq. (1) and Eq. (2).

$$\nabla \cdot U = 0 \tag{1}$$

$$\frac{\partial(\rho U)}{\partial t} + \nabla \cdot (\rho U U) = -\nabla \mathrm{p} + \nabla \cdot \mathrm{S} + \rho f_b \tag{2}$$

where f_b represents the vector with external forces, S represents the viscous stress tensor.

The air and water phases of the numerical model are captured using the two-phase volume of fluid (VoF) technique. The phase volume fraction, α, for air is $\alpha = 0$ and water is $\alpha = 1$. The multiphase formulation with air-water is then treated as a single fluid in the following way

$$\rho = \alpha \rho_{water} + (1-\alpha)\rho_{air} \tag{3}$$

$$\mu = \alpha \mu_{water} + (1-\alpha)\mu_{air} \tag{4}$$

The conservation of the above formulation of the two-phase fraction is given by,

$$\frac{\partial \alpha}{\partial t} + \nabla.(U\alpha) + \nabla.\big(U_c \alpha (1-\alpha)\big) = 0 \tag{5}$$

In the above expression, U_c, represents the artificial compression term given as $U_c = C_\alpha |U| \frac{\nabla \alpha}{|\nabla \alpha|}$. The artificial compression term limits numerical diffusion and preserves a sharp air-water interface within the VoF formulation. The $k - \omega$ Shear Stress Transport (SST) turbulence model is used to capture turbulence effects and predict flow behavior. The $k-\omega$ SST model can be used in the wall through the viscous sub-layer by using a $k-\omega$ formulation in the inner portions of the boundary layer. The $k-\omega$ SST model behaves well in adverse pressure gradients and separating flows. The equations for SST turbulence models for turbulent kinetic energy, k, and turbulence specific dissipation are given in Eqs. (6) and (7),

$$\frac{D}{Dt}(\rho k) = \nabla.(\rho D_k \nabla k) + \rho G - \frac{2}{3}\rho k(\nabla.U) - \rho\beta^*\omega k + S_k \tag{6}$$

$$\frac{D}{Dt}(\rho\omega) = \nabla.(\rho D_\omega \nabla\omega) + \frac{\rho\gamma G}{\nu} - \frac{2}{3}\rho\gamma\omega(\nabla.U) - \rho\beta\omega^2 - \rho(F_1 - 1)CD_{k\omega} + S_\omega \tag{7}$$

where F_1 is the blending function given by,

$$F_1 = tanh\left\{\left\{min\left[max\left(\frac{\sqrt{k}}{\beta^*\omega y}, \frac{500\upsilon}{y^2\omega}\right), \frac{4\sigma_{\omega 2}k}{CD_{k\omega}y^2}\right]\right\}^4\right\} \tag{8}$$

The value of F_1 is maintained at 1 inside the boundary layer and 0 in the free stream.

Computational Domain and Grid Discretization

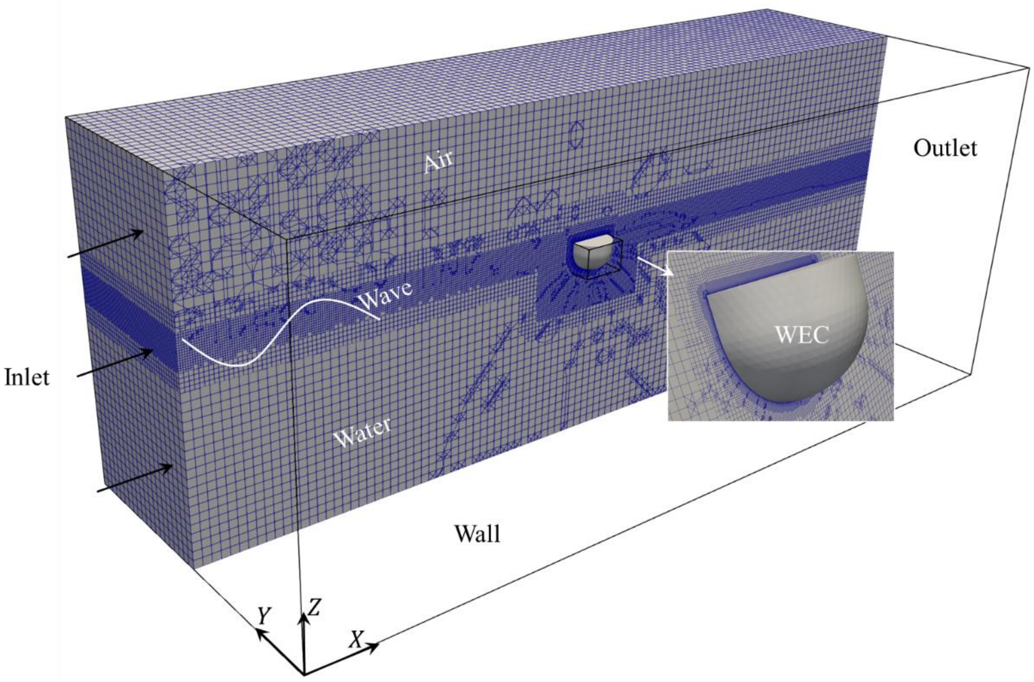

Figure 1. Computation domain with mesh

Figure 1 illustrates the boundary condition and grid discretization of the domain for a reference model with dimensions 200D × 80D high × 80D wide. Heave-dominated WEC device with a hemispherical bottom is considered as highlighted in the computational domain. The point absorber is modeled as an unmoored hemispherical cylinder with diameter, D, a height of $h = 0.675D$ and density, $\rho = 0.84\rho_w$. The draft and freeboard of the body are 0.585D and 0.09D respectively. The water depth is maintained at 45D to ensure a deep-water condition, $d/\lambda \geq 0.5$, where d and λ denote the water depth and wavelength, respectively. The symmetric geometry simplifies hydrodynamic analysis while retaining nonlinear effects such as overwash and vortex shedding. Recent advancements have demonstrated that CFD-based numerical wave tanks can effectively model complex hydrodynamic interactions in multi-DOF WEC systems. The ability to incorporate advanced turbulence modeling and nonlinear wave-structure interactions within OpenFOAM-based solvers has proven effective in accurately predicting WEC behavior under extreme wave conditions (Windt et al., 2018).

SnappyHexMesh toolbox in OpenFOAM 2312 is used to discretize the computational domain to generate structured grids. The grids are refined near the boundary of the WEC and the interface of air and water to capture the wave motion. The waves are generated using a waveVelocity boundary condition, based on the Stokes second-order wave model with a wave height of 3m and a period of 5 seconds. This method computes the velocity of the wave particles, which vary over time and space. A pressure outlet with zero Pascal relative pressure is used at the outlet. The moving wall velocity condition is applied to the WEC to set the velocity during mesh motion, while the seabed is modeled with a no-slip wall condition. Interfoam solver with Crank-Nicolson solver, 2nd-order time-integrator for dynamic mesh modeling simulates 6 DoF WEC motion and the wave energy interactions. The numerical model shows good agreement with experimental results by (Penalba et al., 2018; Windt et al., 2020), confirming the negligible impact of hydrodynamic scaling effects on overall dynamics and total loads under operational conditions.

Grid Independence Study

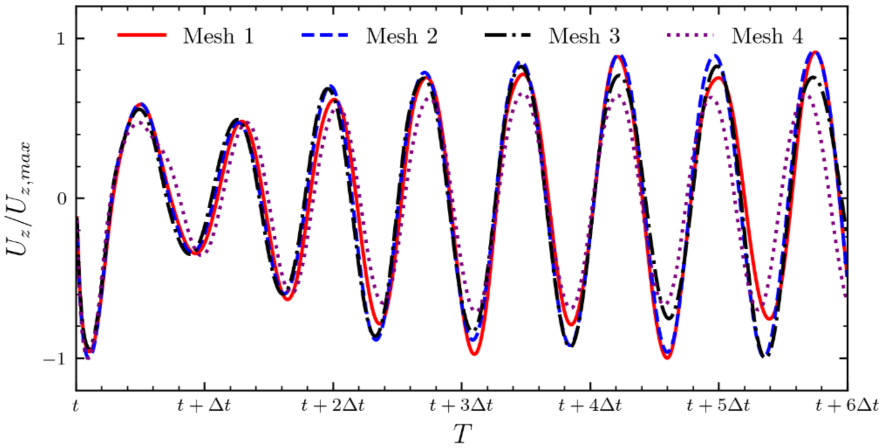

Figure 2. Predicted time histories of heave motion with different grid sizes

Grid generation for a dynamic mesh presents significant challenges to preventing negative volume formation during the dynamic motion of the WEC. To ensure a stable and accurate solution, a structured meshing approach with snappyHexMesh dictionary in OpenFOAM was adopted with targeted refinements. Two distinct refinement regions were defined: one at the air-water interface and the other around the WEC. The initial mesh (Mesh 1) was generated using the blockMesh dictionary with a base grid resolution of 60 × 25 × 25, and the grid size was progressively increased by a factor of 1.2 along all edges. However, simulations with this coarse mesh failed to complete due to the detection of negative volume elements after six oscillations. To mitigate this issue, successive refinements were applied, leading to a stable simulation. Mesh 3 and Mesh 4 configurations utilized blockMesh with edge resolutions of 160 × 100 × 100 and 350 × 120 × 120, ensuring numerical stability and successful completion of the simulation.

Figure 2 illustrates the heave motion of the WEC for different grid resolutions. Mesh 1 - Mesh 4 represents the coarsest to finest meshes, respectively. Each grid was individually assessed to prevent the formation of negative volume elements during oscillations. Although Mesh 1 initially allowed dynamic motion, it eventually failed after six oscillations and was therefore discarded. Mesh 2 and Mesh 3 exhibited comparable oscillatory behavior, indicating sufficient resolution for capturing the dynamics. However, Mesh 4, while providing the highest accuracy, was computationally expensive, making storing all time-step data impractical. Mesh 3 was selected as the optimal grid to balance computational cost and accuracy. A total of ~500 GB of data were collected for this configuration.

RESULTS AND DISCUSSIONS

Six DoF WEC motions

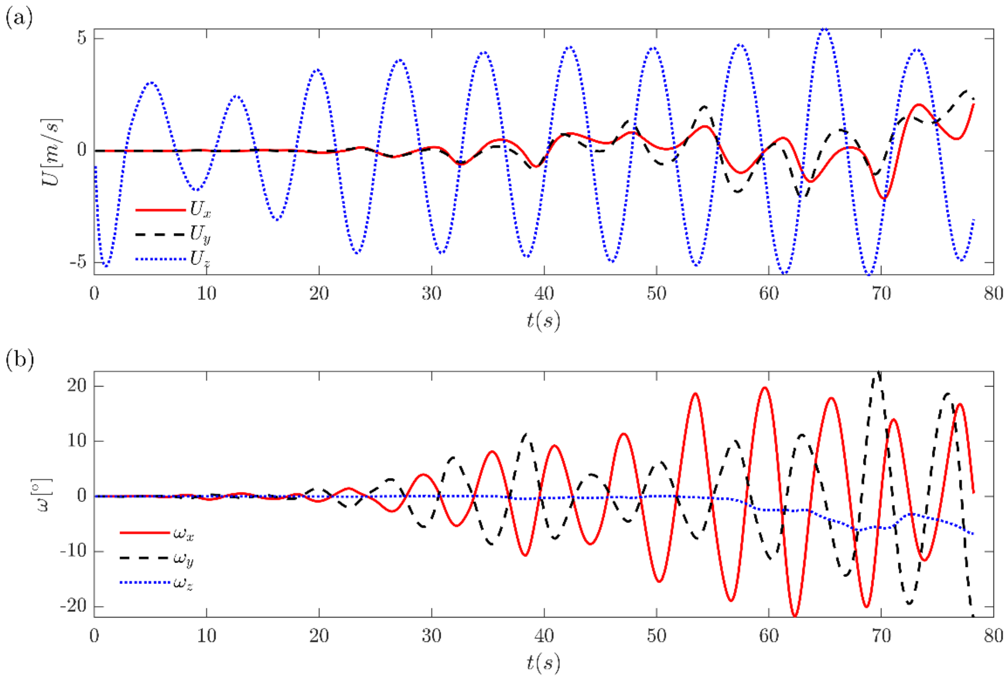

Figure 3. Predicted time histories of (a) WEC velocity and (b) angular motions

During wave–WEC interactions, the predominant motion is along the vertical axis (z-axis for the present numerical model). As shown in Fig. 3, over the 80s simulation, the WEC oscillates mainly along the z-axis. In Fig. 3(a), motions along x and y directions show an initial delay of about 25s, attributed to fluid–structure interaction. As time progresses, motion along all directions is predicted, but with lower amplitudes compared to vertical motion. Similarly, angular motions, yaw, pitch, and roll, are also captured as illustrated in Fig. 3(b). Nonlinear second-order wave kinematics and $3D$ flow separation generate y-velocities comparable to x-velocities despite unidirectional wave input. The hemispherical shape results in significant heave motion, driven by buoyancy and hydrostatic stiffness, leading to larger vertical than horizontal displacements. Moreover, the lack of tethering allows free movement in all directions, although buoyancy forces dominate and result in larger vertical motions.

The physics of the angular motion is similar to that of the translation motion, as illustrated in Fig. 3(b). The angular velocities are expressed in degrees within the body-fixed coordinate system of the WEC, where roll, pitch, and yaw correspond to the rotation along the x, y, and z axes, respectively. For rotational motion, the rotation along the longitudinal axis (ω_x) and transverse axis (ω_y) is dominant. However, the yaw motion (ω_z) decays due to the predominance of vertical translation, which suppresses the rotational response. The interaction shows great dominance of the vertical dynamics with minimal cross-coupling in the translation and angular directions. In the figure, similar magnitudes of pitch and roll arise from the hemispherical geometry, with nearly identical hydrostatic stiffness in both directions. Second-order wave forces excite both motions equally, while the high mass moment of inertia and low stiffness lead to significant angular displacements.

Dynamic Loadings

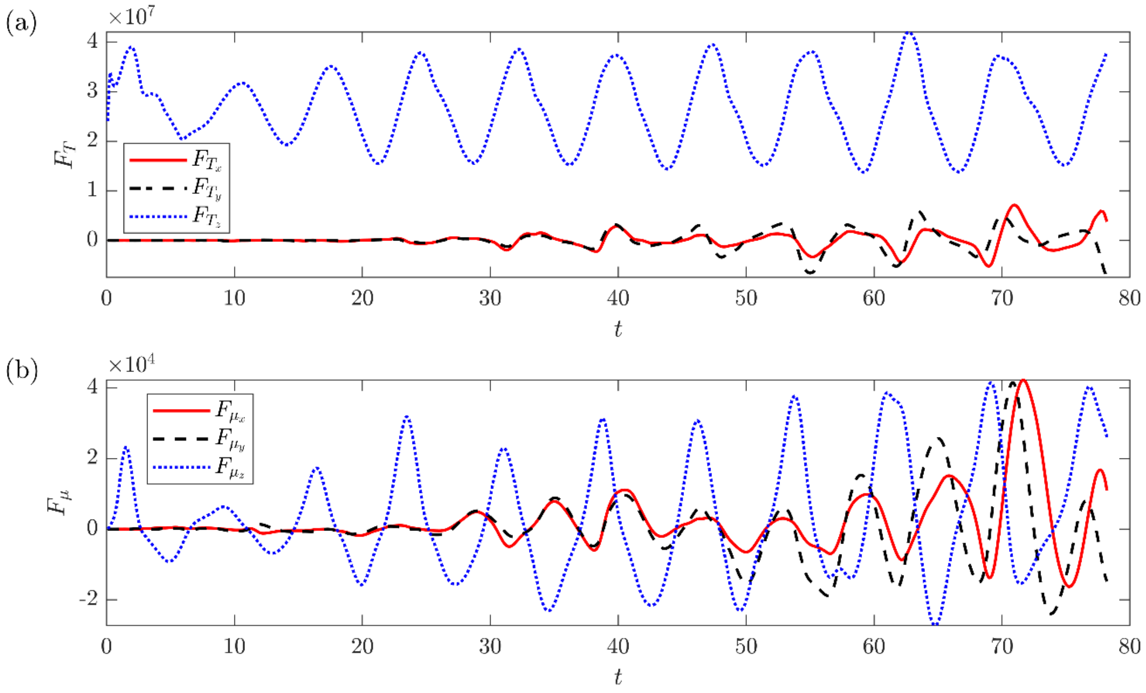

Figure 4. Predicted time histories of forces acting on WEC for (a) total forces and (b) viscous forces

The time histories of the forces acting on the WEC due to WEC-wave interactions for a total time of 80s are indicated in Fig. 4. Figure 4(a) shows the total force acting on the WEC, expressed as ($F_T = F_p + F_\mu$), where the subscripts T, P, μ represents total force, pressure force, and viscous force, respectively. Similar to the observation for WEC motions, the forces acting along the vertical directions are maximum compared to the translation forces (F_{T_x}, F_{T_y}). In Fig. 4 (a), the mean vertical force approximately opposes and equals the magnitude of the gravitational force acting on the point absorber. Regardless of the dominance of vertical motions in the total translational forces, viscous forces have significant contributions in all directions, as illustrated in Fig. 3(b). Moreover, many studies on ocean energy neglect the effect of viscous forces by utilizing the potential flow theory (Babarit, 2013; Gerostathis et al., 2024; Magkouris et al., 2020; Shadmani et al., 2024). Viscous forces have a significantly lower magnitude compared to the total forces acting on WEC; however, utilizing these forces can improve the precision of the power take-off system to capture the energy in all available directions.

Instantaneous Flow Visualization

In Fig. 5, the volume fraction of water-air by applying the VoF method with interface tracking at different times (*T*/4, *T*/2, 3*T*/4, and *T*) is presented. The WEC continues to oscillate in all possible directions. Such interactions influence viscous dissipation, as shown in Fig. 4, leading to significant viscous forces acting on the WEC body. These viscous forces due to wave-WEC interactions contribute to energy losses and cause higher structural stresses on the WEC body. The zoomed-in section in Fig. 5 presents the air-water interface with possible regions of formations of wakes and vortices. These flow regions of high-velocity gradients and shear increase viscous dissipation, which affects the hydrodynamic forces on the WEC and the overall energy capture.

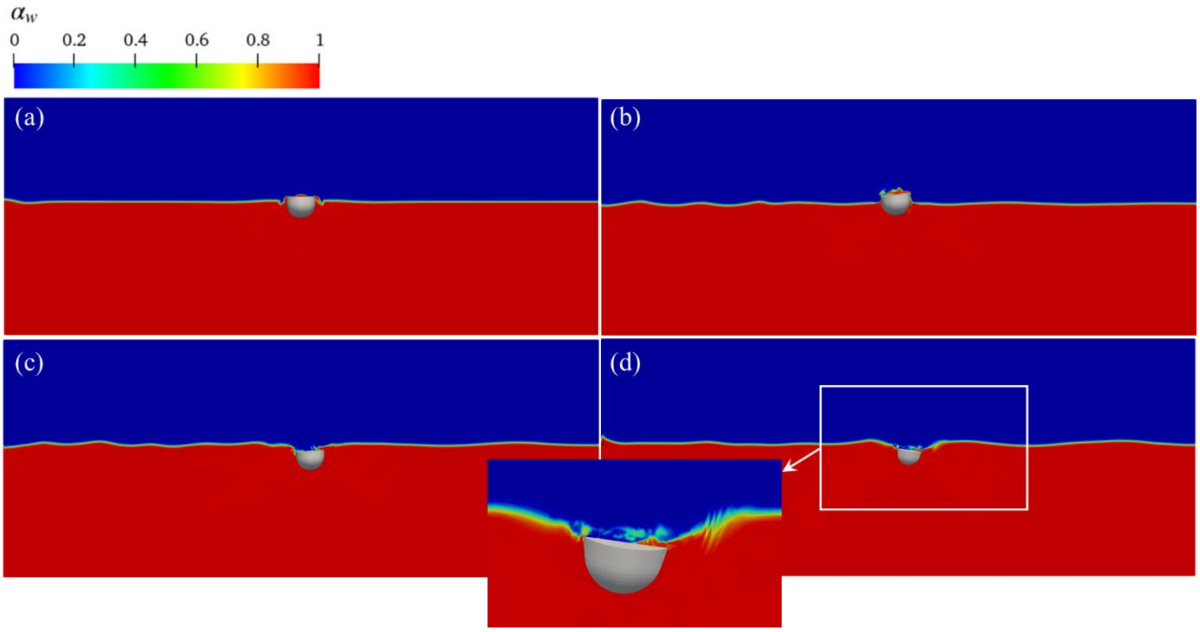

Figure 5. Water-air volume fractions during wave-WEC interactions, where (a)-(d) represent time *T*/4, *T* /2, 3*T* /4, and *T,* respectively

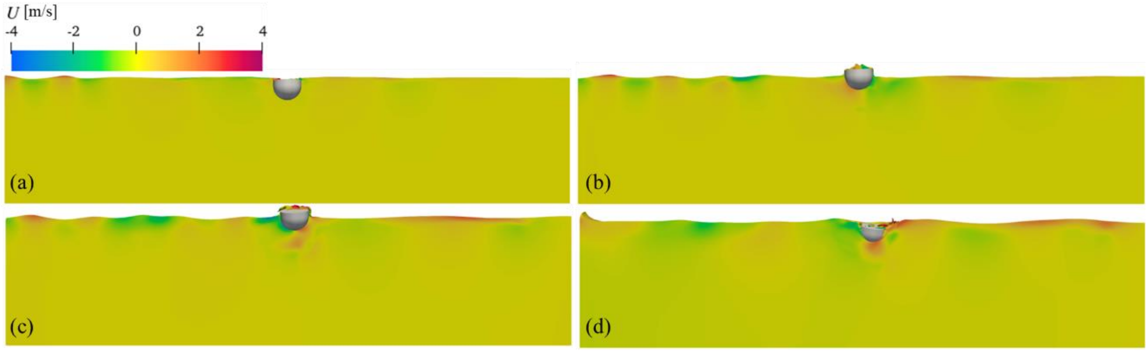

Figure 6. Streamwise instantaneous velocity during wave-WEC interactions, where (a)-(d) represent time *T*/4, *T*/2, 3*T* /4, and *T,* respectively

Figure 6 presents the instantaneous streamwise velocity, isolating the water region with 50% water content. Near the air-water interface, the mixing induced by wave action is visible, indicating significant air-water interaction. Around the WEC, a flow separation region develops, becoming more pronounced as the WEC undergoes oscillation, as illustrated in Fig. 6(d). This oscillation also initiates small-scale entrainment of the surrounding fluid, contributing to further air-water mixing within the core wake region. As the WEC oscillates, downstream vortices roll up and merge with the core region, intensifying the wake dynamics.

CONCLUSIONS

The 6 DoF motion of WEC was investigated using a numerical technique with RANS k-ω SST turbulence model. A VoF method was utilized to capture air-water interactions. The results showed that the WEC motion is predominantly along the vertical axis with delayed and lower amplitude across translational and rotational directions. The effects of viscous forces acting on the WEC were also examined. While pressure forces dominate the vertical motion, viscous forces contribute significantly to the energy dissipation in all directions. The wake and vortex formations near the air-water interface were observed, which intensify viscous dissipation and affect the hydrodynamic forces on the WEC. Considering these forces improves the precision of the PTO systems to optimize the energy captured. The present study considers a free-floating point absorber. In addition, small-scale vortices may be under-resolved due to using unsteady RANS instead of higher-fidelity numerical simulations. Future work will incorporate tether force modeling, extend simulations to multi-directional and irregular waves, improve wave absorption techniques, and validate the results against experimental data to improve the accuracy of WEC motion predictions.

ACKNOWLEDGEMENTS

The authors express their sincere appreciation for the financial support provided by the Natural Sciences and Engineering Research Council of Canada, and the Office of the Vice-President (Research) at Memorial University of Newfoundland. Additionally, they acknowledge the support of the Supercomputing Facility through the Digital Research Alliance of Canada.

REFERENCES

Babarit, A., 2013. On the park effect in arrays of oscillating wave energy converters. Renewable Energy 58, 68–78. https://doi.org/10.1016/j.renene.2013.03.008

Gallutia, D., Tahmasbi Fard, M., Gutierrez Soto, M., He, J., 2022. Recent advances in wave energy conversion systems: From wave theory to devices and control strategies. Ocean Engineering 252, 111105. https://doi.org/10.1016/j.oceaneng.2022.111105

Galván-Pozos, D.E., Ocampo-Torres, F.J., 2020. Dynamic analysis of a six-degree of freedom wave energy converter based on the concept of the Stewart-Gough platform. Renewable Energy 146, 1051–1061. https://doi.org/10.1016/j.renene.2019.06.177

Gerostathis, T., Magkouris, A., Belibassakis, K., 2024. A 3D BEM-Coupled Mode Model for the Performance Analysis of Wave Energy Converter Parks in Nearshore-Coastal Regions. JMSE 12, 212. https://doi.org/10.3390/jmse12020212

Lehmann, M., Karimpour, F., Goudey, C.A., Jacobson, P.T., Alam, M.-R., 2017. Ocean wave energy in the United States: Current status and future perspectives. Renewable and Sustainable Energy Reviews 74, 1300–1313. https://doi.org/10.1016/j.rser.2016.11.101

Li, Y., Yu, Y.-H., 2012. A synthesis of numerical methods for modeling wave energy converter-point absorbers. Renewable and Sustainable Energy Reviews 16, 4352–4364. https://doi.org/10.1016/j.rser.2011.11.008

Magkouris, A., Bonovas, M., Belibassakis, K., 2020. Hydrodynamic Analysis of Surge-Type Wave Energy Devices in Variable Bathymetry by Means of BEM. Fluids 5, 99. https://doi.org/10.3390/fluids5020099

Penalba, M., Davidson, J., Windt, C., Ringwood, J.V., 2018. A high-fidelity wave-to-wire simulation platform for wave energy converters: Coupled numerical wave tank and power take-off models. Applied Energy 226, 655–669. https://doi.org/10.1016/j.apenergy.2018.06.008

Ransley, E.J., Greaves, D., Raby, A., Simmonds, D., Hann, M., 2017a. Survivability of wave energy converters using CFD. Renewable Energy 109, 235–247. https://doi.org/10.1016/j.renene.2017.03.003

Ransley, E.J., Greaves, D.M., Raby, A., Simmonds, D., Jakobsen, M.M., Kramer, M., 2017b. RANS-VOF modelling of the Wavestar point absorber. Renewable Energy 109, 49–65. https://doi.org/10.1016/j.renene.2017.02.079

Shadman, M., Estefen, S.F., Rodriguez, C.A., Nogueira, I.C.M., 2018. A geometrical optimization method applied to a heaving point absorber wave energy converter. Renewable Energy 115, 533–546. https://doi.org/10.1016/j.renene.2017.08.055

Shadmani, A., Nikoo, M.R., Gandomi, A.H., 2024. Adaptive systematic optimization of a multi-axis ocean wave energy converter. Renewable and Sustainable Energy Reviews 189, 113920. https://doi.org/10.1016/j.rser.2023.113920

Vervaet, T., Stratigaki, V., De Backer, B., Stockman, K., Vantorre, M., Troch, P., 2022. Experimental Modelling of Point-Absorber Wave Energy Converter Arrays: A Comprehensive Review, Identification of Research Gaps and Design of the WECfarm Setup. JMSE 10, 1062. https://doi.org/10.3390/jmse10081062

Windt, C., Davidson, J., Ransley, E.J., Greaves, D., Jakobsen, M., Kramer, M., Ringwood, J.V., 2020. Validation of a CFD-based numerical wave tank model for the power production assessment of the wavestar ocean wave energy converter. Renewable Energy 146, 2499–2516. https://doi.org/10.1016/j.renene.2019.08.059

Windt, C., Davidson, J., Ringwood, J.V., 2018. High-fidelity numerical modelling of ocean wave energy systems: A review of computational fluid dynamics-based numerical wave tanks. Renewable and Sustainable Energy Reviews 93, 610–630. https://doi.org/10.1016/j.rser.2018.05.020

Yang, I., Tezdogan, T., Incecik, A., 2023. Numerical investigations of a pivoted point absorber wave energy converter integrated with breakwater using CFD. Ocean Engineering 274, 114025. https://doi.org/10.1016/j.oceaneng.2023.114025